Volume 1 | Number 1 | Jan 2013 | Pages 1–100

Journal of
Materials Chemistry A

Materials for energy and sustainability
www.rsc.org/materialsA

Li⁺

ROYAL SOCIETY
OF CHEMISTRY

ROYAL SOCIETY
OF **CHEMISTRY**
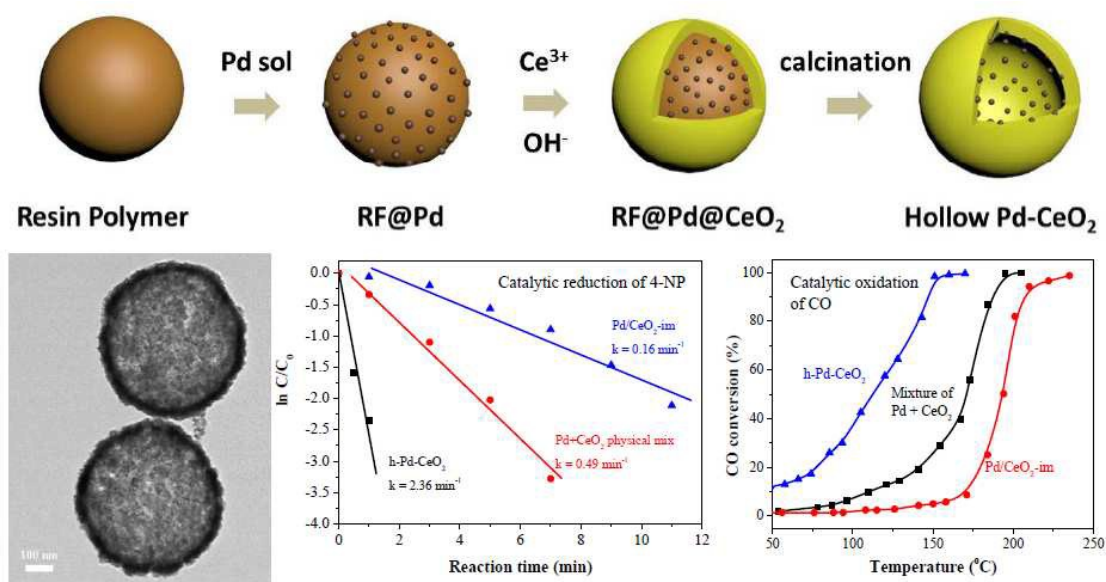
www.rsc.org/materialsA

Graphic abstract:

Polymer-templated synthesis of hollow Pd-CeO₂ nanocomposite spheres and its catalytic activity and thermal stability

Chenhao Du, Yun Guo, Yanglong Guo, Xue-qing Gong, Guanzhong Lu[*]

Key Laboratory for Advanced Materials and Research Institute of Industrial Catalysis, East China University of Science and Technology, Shanghai 200237, P. R. China.

Polymer-templated synthesis of hollow Pd-CeO$_2$ nanocomposite spheres and its catalytic activity and thermal stability

Chenhao Du, Yun Guo, Yanglong Guo, Xue-qing Gong, Guanzhong Lu[*]

Key Laboratory for Advanced Materials and Research Institute of Industrial Catalysis, East China University of Science and Technology, Shanghai 200237, P. R. China.

* Corresponding author: Fax: +86-21-64252923, E-mail: gzhlu@ecust.edu.cn (G.Z. Lu)

Abstract: The developing methods to fabricate active and thermal-stable noble metal/metal oxide nanomaterials are very important for the catalysis and material fields. Herein, we used a polymer-template synthesis approach to prepare hollow Pd-CeO$_2$ nanocomposite spheres (NCSs) with Pd nanoparticles evenly distributed inside the CeO$_2$ shell, in which the aggregation of Pd nanoparticles can be well inhibited by the help of the protection of CeO$_2$ nanocrystallites even after being calcined at 700 °C. The Pd nanoparticles are partially buried in the CeO$_2$ shell and the surface Pd species are highly ionic, which is caused by the electron exchange at the Pd-CeO$_2$ interface during calcination. This hollow structure Pd-CeO$_2$ nanocatalyst shows the excellent catalytic activity and stability in the aqueous selective reduction of 4-nitrophenol and gaseous CO oxidation. Compared to the supported Pd/CeO$_2$ and physical mixed Pd + CeO$_2$ catalysts, the reaction rate over this h-Pd-CeO$_2$ NCSs catalyst is almost 14 times and 5 times faster for the selective reduction of 4-nitrophenol, respectively. For the CO oxidation, the larger Pd-CeO$_2$ interface in h-Pd-CeO$_2$ NCSs

could facilitate the reaction between adsorbed CO and O_2, thus showing a better low temperature activity. This paper emphasizes the advantages of core-shell hollow structure and provides a new way to obtain novel functional nanocatalysts.

Keywords: Hollow structure materials; Pd-CeO_2 nanocomposite; Selective reduction of 4-nitrophenol; CO oxidation; Nano-catalysis materials.

1. Introduction

Noble metal nanoparticles (NPs) have been extensively researched in the field of catalysis in recent years, due to their high-effectively catalytic performances [1-3]. It is well known that, the catalytic activity of noble metal NPs is closely dependent on their composition, size, shape and crystallinity [4-7]. However, owing to their high surface area and surface energy, noble metal NPs tend to aggregate to larger particles to minimize their surface energy, especially during the catalytic reaction at high temperature, which could easily lead to its deactivation or loss of the catalytic activity [8,9]. To solve these problems, isolating noble metal NPs in small cavities is a reasonable solution, because it can efficiently prevent particles migration and its deactivation. Besides, this isolating method can also reduce the leaching of the active components from the catalyst particles in the chemical processes, which is another important aspect in a design of new nano-catalysts [10, 11].

To isolate noble metal NPs, the porous inert oxide coating and core-shell hollow nanostructures are the ideal solution approaches, and both have been widely researched recently [12-20]. Liu *et al*. designed a coking- and sintering-resistant palladium catalyst by an atomic layer deposition method, which can enhance the catalytic activity and stability of Pd/Al_2O_3 catalyst for the oxidative dehydrogenation of ethane [18]. Zhang *et al*. reported the graphene nanosheet-supported ultrafine metal nanoparticles encapsulated by thin mesoporous SiO_2 layers, which exhibited the remarkable high-temperature stability [19]. Similarly, porous silica-coated Pt NPs on carbon nanotube possessed the good thermal stability for the hydrogenation of nitrobenzene [20]. However, Al_2O_3 or SiO_2 are unreactive component and only play a dispersion role, and the synergistic effect between noble

metal NPs and (Al_2O_3 or SiO_2) layer is quite weak. From a viewpoint of heterogeneous catalysis, especially for metal/metal oxide catalysts, the interaction between the metal nanoparticles and reactive support [21-23], such as CeO_2 and TiO_2, are quite vital for improving the reactivity and stability of the catalysts.

As one of the most commonly used reducible oxides, ceria possesses the high oxygen storage capacity and redox property, and plays an important role in the field of catalysis and has been researched extensively [24-27]. Although various methods for the fabrication of hollow ceria spheres have been reported [28-30], the research on CeO_2-containing nanocomposite hollow spheres, especially composite with noble metals nanoparticles, are relatively rare. For example, Liu and co-workers designed a nano-reactor with noble metal NPs decorated in the inner walls of the CeO_2 shells and showed that it could enhance the catalytic activity and stability [31]. Xu *et al*. synthesized hollow Pd@CeO_2 sphere by core-shell protocol, which exhibited the excellent reusable and higher catalytic performance for the thermocatalytic and photocatalytic selective reduction of aromatic nitro compounds [32]. However, these researches only were involved with the catalytic processes at ambient conditions, and the high-temperature stability of these catalysts was not demonstrated, which are very important for the gas-solid phase catalytic reaction at higher temperature. Therefore it is quite necessary to develop the novel nanocatalysts with good activity and stability for both gas- and liquid-phase reactions.

Herein, we reported the fabrication of hollow Pd-CeO_2 nano-composite spheres (NCSs) by a facile hard-template method in aqueous phase, followed by the elimination of the polymer templates by simple calcination. In this hollow Pd-CeO_2 NCSs, the aggregation of Pd nanoparticles can be efficiently avoided by the protection of the CeO_2 crystal. The high dispersity of Pd species can be well maintained even after calcination at 700 °C. The synthesized hollow Pd-CeO_2 NCSs exhibits highly catalytic activity for the selective reduction of aromatic nitro compounds at ambient conditions and the CO oxidation. It is the most important that hollow Pd-CeO_2 NCSs possesses highly thermal stability and reusability compared with conventional supported Pd/CeO_2 catalyst.

2. Experimental section

2.1. Preparation of samples

Monodispersed resorcinol-formaldehyde (RF) polymer sphere. RF polymer spheres were synthesized [33]. Typically, 0.1 mL of ammonia aqueous solution (NH$_4$OH, 25wt%) was mixed with a solution containing 8 mL ethanol and 20 mL de-ionized water. After stirring for 1h, 0.1 g resorcinol was added to this mixed solution and it was continually stirred for 30 min. Then 0.14 mL formaldehyde solution was added and stirred for 24 h at 30 °C, and subsequently this synthesis solution was transferred to the Teflon-lined stainless autoclave and treated at 100 °C for 24 h. The as-synthesized product was collected by centrifugation and washed with de-ionized water twice. Finally, the solid product was dried in air at 100 °C for 24h.

PVP-protected Pd nano-particles. PVP-protected Pd nanoparticles were prepared by alcohol reduction method [34]. H$_2$PdCl$_4$ aqueous solution (2 mM) was prepared by mixing 106.4 mg PdCl$_2$, 6 mL 0.2 M HCl and 294 mL ultrapure water. A mixed solution of 15 mL H$_2$PdCl$_2$ aqueous solution, 21 mL de-ionized water, 14 mL ethanol and 66.7 mg PVP was refluxed in a 100 mL flask at 90 °C for 3 h. The obtained dark-brown PVP-protected Pd colloidal solution was stable at room temperature for months.

Hollow Pd-CeO$_2$ nano-composite (h-Pd-CeO$_2$). 25 mg of as-prepared RF spheres was dispersed in 20 mL de-ionized water under ultra-sonication to obtain a homogeneous dispersion, followed by adding the Pd colloidal solution (10-15 μmol). This mixture was stirred for 4-6 h to allow Pd NPs fully deposited on the surface of RF spheres, to form RF@Pd structure. Then mixed solution of 0.15 g CeCl$_3$, 0.085 g hexamethylenetetramine (HTMA) and 20 mL de-ionized water was added into the solution mentioned-above containing RF@Pd particles, and it was continually stirred for 15 min. Then this synthesis solution was transferred into a 100 mL of Teflon-lined stainless autoclave and treated at 100 °C for 6 h. The obtained products were separated by centrifugation, washed with de-ionized water 3 times to remove unreacted residues, and then dried at 60 °C overnight and calcined at 500-700 °C for 2 h in a muffle furnace.

The Pd/CeO$_2$ catalyst. The supported Pd/CeO$_2$ was prepared by the conventional impregnation method (Pd/CeO$_2$-imp), and the Pd loading was ~2.0 wt.%. Commercial CeO$_2$ powder was provided by Aladdin Company. The as-synthesized Pd/CeO$_2$ powder was calcined at 500 °C for 2 h.

The physical mixture of Pd + CeO$_2$. The 2.0 wt.%Pd physical mixed sample was prepared by an evaporation of the colloid solution including CeO$_2$ nanoparticles and Pd nanoparticles and followed by calcination in air at 500 °C for 2h.

2.2. Catalytic activity testing

The selective reduction of 4-nitrophenol. Catalytic performance of the catalyst for the selective reduction of 4-nitrophenol was tested as follows. Typically, the catalyst (1.5 mg) was added into 40 mL ultrapure water in a 100 mL beaker to form a homogeneous dispersion under ultrasonication for 10 min, and then 0.5 mL of freshly prepared 0.5M NaBH$_4$ aqueous solution was added. After stirring for a few seconds at room temperature, 4-nitrophenol (0.012 M, 0.25 mL) was added into the reactor at room temperature (25 °C). The reaction process was monitored by direct color change of the solution. At different reaction times, 1.5 mL of solution was withdrawn by a syringe and filtered by 0.22 μm Millpore film, and the reaction solution was analyzed by the UV−Vis spectroscopy.

Recycling of catalyst. After the reaction ended, the catalyst was separated by centrifugation at 5000 rpm for 10 min, and the catalyst was dried at 60 °C. Then this catalyst was directly reused under the same reaction conditions.

The CO oxidation. The catalytic activity of the sample for CO oxidation was evaluated at atmosphere pressure in a quartz tubular reactor. 30 mg of catalyst was mixed with 200 mg silica (40-60 mesh). The total flow rate of the feed gas of 1%CO-20%O$_2$/N$_2$ was 50 mL/min. The catalyst was pretreated in N$_2$ at 150 °C for 1 h and then the temperature was raised at a rate of 2 °C/min. The gas composition was monitored online by the gas chromatograph (GC 2060 system) with a flame ionization detector (FID) and methanation reactor. The conversion of CO was calculated on the basis of the change of CO concentrations in the inlet and outlet gases.

2.3. Characterization of samples

Elemental analysis of the sample was done by inductively coupled-plasma atomic emission spectroscopy (ICP-AES) on a Varian 710ES instrument (Varian Co. Palo Alto, US). Powder X-ray diffraction (XRD) patterns were recorded on a PANalytical PW 3040/60 X'Pert Pro powder diffractometer with CuKα radiation, which was operated at 40 kV and 40 mA and a scanning speed was 0.5°/min. Thermogravimetric (TG) analysis was conducted on a Pyris diamond thermal analyzer at a heating rate of 10 °C/min from room temperature to 800 °C. The surface areas of samples were measured by N_2 adsorption/desorption at –196 °C on a micromeritics ASAP 2020 instrument, and calculated by the Brunauer–Emmett–Teller (BET) method.

Transmission electron microscopy (TEM) images and energy dispersive X-ray spectroscopy (EDX) were taken on a JEM-1400 & JEM-2100 transmission electron microscope. The sample was ultrasonically suspended in the ethanol solvent, and one or two drops of this slurry was deposited on a copper grid. The liquid phase was evaporated before the grid was loaded into the microscope. Scanning electron microscopy (SEM) images were taken on a Hitachi S-3400 scanning electron microscope operated at 15 kV and using secondary electrons to form the images. The sample was coated with a thin layer of gold before testing.

X-ray photoelectron spectroscopy (XPS) spectra of samples were obtained on a Kratos Axis Ultra-DLD photoelectron spectrometer equipped with AlKα (1486.6 eV) radiation as the excitation source. All binding energies (BE) were determined with respect to the C1s line (284.6 eV) originating from adventitious carbon.
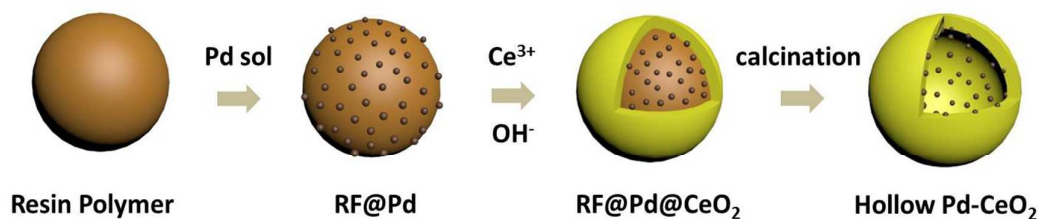
Scheme 1. The formation process of hollow Pd-CeO$_2$ nano-composite sphere.

3. Results and discussion

3.1. Preparation of hollow Pd-CeO$_2$ nanocomposite spheres and their properties

The synthesis process of hollow Pd-CeO$_2$ nanocomposite spheres (NCSs) is illustrated in Scheme 1. The pre-synthesized Pd colloidal nano-particles (NPs) with PVP as stabilizer are 2.5−3 nm (Figure S1), and could be loaded on the surface of monodispersed resin polymer spheres by the π-π interaction between the polymer template and PVP (Figure S2) [32,35]. Basically, almost all of the Pd colloidal nanoparticles are successfully deposited on the surface of polymer, which can be verified by the relative colorless transparent supernatant obtained after centrifugation of the RF@Pd suspension. As is well known, hexamethylenetetramine (HTMA) can hydrolyze in water to give NH$_3$ [36], while the basicity of the solution is slowly changed during the reaction, which ensures the slow hydrolysis of CeCl$_3$ and condensation of Ce^{3+} ions. Meanwhile, with the coordination effect of PVP and surface functional groups on polymer surface, CeO$_2$ could be well deposited on the template surface to form RF@Pd@CeO$_2$ core-shell structure. Followed by calcination in air, the RF template and PVP are removed and the hollow CeO$_2$ shell forms simultaneously.

As shown in Figure 1, the diameter of mono-dispersed RF resin polymer spheres is ~500 nm, and well-structured hollow spheres and the inner hollow structure can be clearly observed as indicated with the arrows (Figure 1b), which is further confirmed by the TEM image (Figure 1c). The CeO$_2$ shells composed of sub-10 nm CeO$_2$ nanocrystallites with the thickness of ~35 nm, and the cavities in the shell can guarantee the reagents diffusion and contact in the inner and outer surfaces of the shell during the catalytic reaction. No bare Pd NPs are spotted on the surface of hollow spheres and almost all of the Pd NPs are embedded in the CeO$_2$ nanocrystals after calcination, forming Pd-CeO$_2$ interfaces as indicated by the white arrow (Figure 1d). The TG analysis shows that the hollow Pd-CeO$_2$ NCSs behaves hardly weight loss at 100−800 °C, which demonstrates the complete elimination of resin polymer spheres during the calcination (Figure S3).
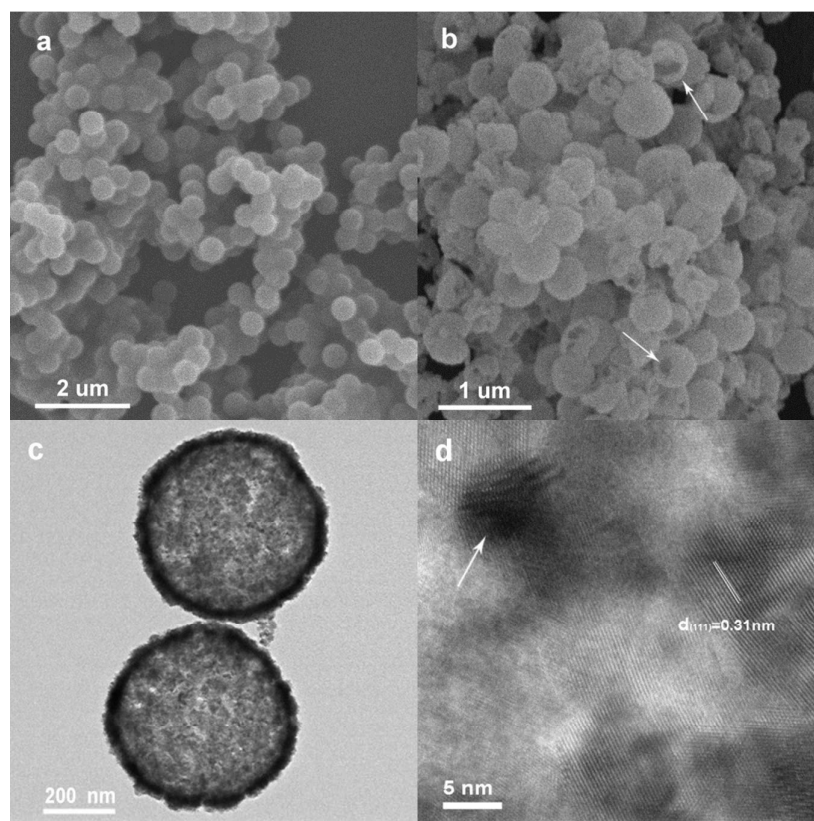
Figure 1. SEM images of (a) resin polymer template and (b) SEM, (c) TEM, (d) HR-TEM of hollow Pd-CeO$_2$ NCSs calcined at 773K.
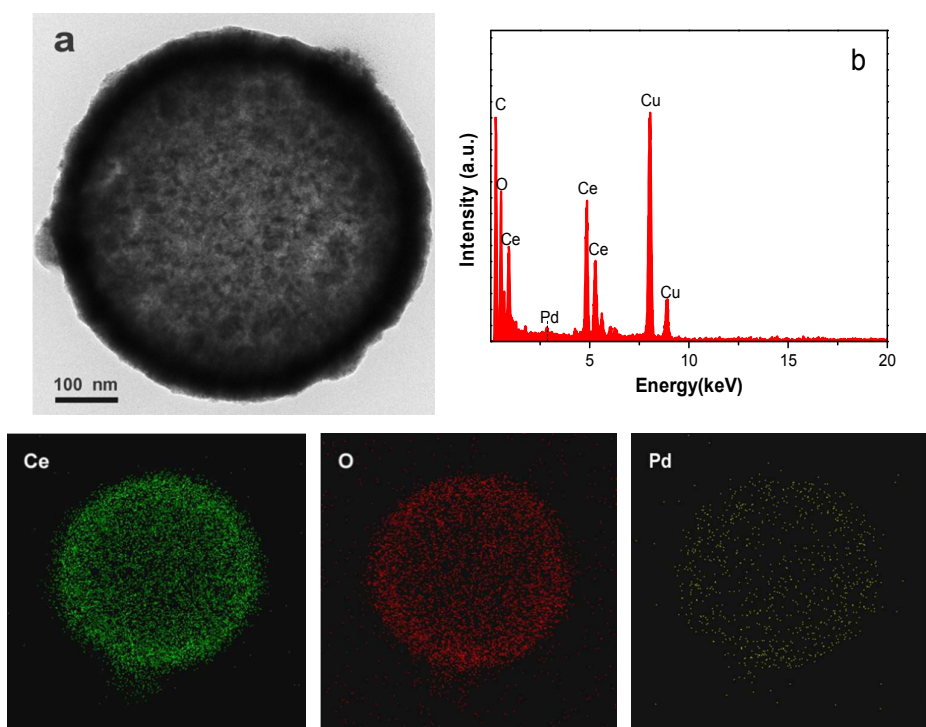

Figure 2. (a) TEM images, (b) EDX spectra of individual hollow Pd-CeO$_2$ NCS calcined at 500 °C, and its element mappings of Ce, O and Pd.

8

Owing to the high electron density of polycrystalline CeO_2 and the hollow shell structure, it is difficult to identify Pd NPs located on the ceria shell. To visualize the spatial distribution of Pd species, we used the EDX technique to analyze the individual hollow $Pd-CeO_2$ sphere, and the results are shown in Figure 2. It can be seen that the elements of Pd, Ce and O spread evenly on whole sphere, which proves that no Pd aggregation appeared on the CeO_2 shell. Besides, the composition line-scan profiles across a single $h-Pd-CeO_2$ nanocomposite sphere were obtained by means of SEM-EDX and shown in Figure S4, which indicates that all elements (Ce, O and Pd) are distributed throughout the sphere.
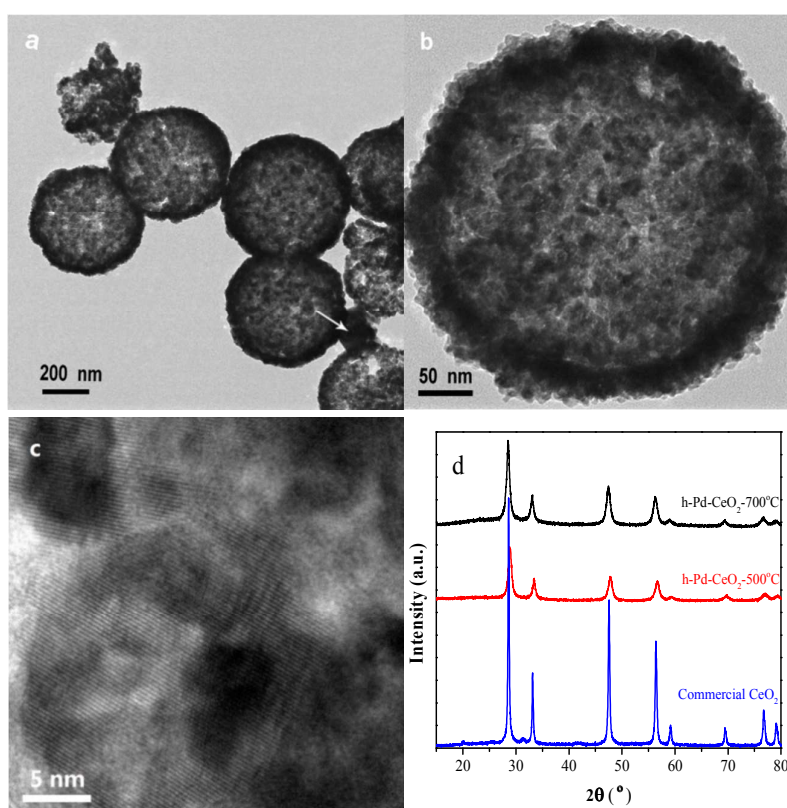
Figure 3. (a, b, c) TEM images spectra of hollow $Pd-CeO_2$ NCSs calcined at 700 °C, (d) XRD profile of CeO_2 and $h-Pd-CeO_2$ NCSs.

As shown in the XRD spectra (Figure 3d), the hollow $Pd-CeO_2$ NCSs are the polycrystalline structure, the diffraction peaks result from CeO_2, and no diffraction peaks of Pd or Pd oxide could be observed, probably due to relative low content or high dispersion of Pd species in the sample. With an increase in the calcination temperature from 500 to 700 °C, the hollow structure is well

maintained and no Pd NPs or aggregated Pd particles were observed in its TEM images (Fig. 3(a-c));

the diffraction peaks become slightly narrower, while the size of CeO_2 crystallites increases from

5-10 to 10-15 nm and its BET surface area decreases from 59.3 to 33.9 m^2/g (Table S1). As shown

in Fig. 3b, the shell is more rugged and this hard-template method can effectively inhibit the crystal

size growth at higher temperature, whereas isolated CeO_2 nano-particles would severely aggregate

as indicated by the white arrow in Figure 3a. Comparing with the supported Pd/CeO_2 catalyst (9.1

m^2/g), the hollow $Pd-CeO_2$ NCSs has a larger surface area (33.9 m^2/g) after calcination at 700 °C

(Table S1).

The hollow $Pd-CeO_2$ NCSs have also been investigated by the XPS technique, and the results are

shown in Figure 4. In the Pd $3d_{5/2}$ and $3d_{3/2}$ XPS spectra, two peaks are located at ~337.6 eV and

342.9 eV respectively. In general, the BE (Binding Energy) values of Pd $3d_{5/2}$ in PdO species are in

the range of 336−337.2 eV, so that the Pd in the hollow $Pd-CeO_2$ NCS should not be PdO. It was

reported that, the fact that the XPS peaks of Pd^{2+} shifted to higher BE value in Pd/CeO_2, could be

explained by the formation of solid solution-like $Pd_xCe_{1-x}O_2$ structure, in which the Pd^{2+} ions

replaced the Ce^{4+} ions in the CeO_2 crystalline lattice [37-40]. This result demonstrates that the Pd NPs

are embedded inside the CeO_2 nanocrystals, but not completely buried in the ceria shell. A fraction

of Pd atoms located at the $Pd-CeO_2$ interface are exposed and the electron exchange between Pd

atoms and CeO_2 matrix leads to the formation of ionic Pd species. Besides, the previous researches

showed that the Pd^{2+} ions could not be completely reduced and minor Pd^{2+} component might exist

on the surface of Pd NPs [41,42]. Thus, on the basis of XPS data and the $Pd-CeO_2$ interface observed

in Figure 1d, we can consider that the chemical state of surface Pd in the hollow $Pd-CeO_2$ NCSs is

mainly ionic Pd^{2+} but not in the form of PdO, which probably results from the strong metal-support

interaction caused by the treatment at high temperature, and forming the solid solution-like

$Pd_xCe_{1-x}O_2$ structure.

For the $Pd-CeO_2$ NCSs, after being calcined at 700 °C, its valence state of Pd species is

unchanged, but the intensities of peaks are stronger than those of the sample calcined at 500 °C

(Figure S5), which indicates that the surface concentration of Pd species increased after calcination

at higher temperature (Table 1). This phenomenon is caused probably by two reasons. (1) Small Pd

nanoparticles would undergo a structural evolution and the Pd atoms could dissociate from Pd

nanoparticles in the process of calcination at 800 °C, but this situation would not occur at 500 °C [43].

Thus, in the h-Pd-CeO₂ NCSs, some Pd atoms may dissociate and incorporate into the CeO₂

nanocrystallites during the calcination at 700 °C, which causes an increase in the concentration of

surface Pd species, though the Pd NPs remain in their original places. (2) After calcination at

700 °C, the growth of CeO₂ nanocrystallites leads to the surface shrinkage of ceria hollow sphere

and an decrease in its surface area (from 59.3 to 33.9 m^2/g, Table S1). Thus the Pd NPs number per

square meter would increase, resulting in the higher surface concentration of Pd species for the

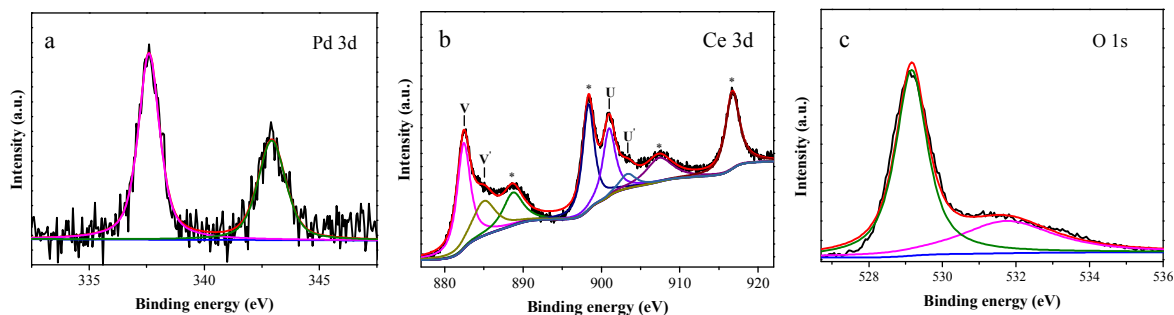sample calcined at 700 °C than that of the sample calcined at 500 °C.

Figure 4. XPS spectra of (a) Pd 3d, (b) Ce 3d and (c) O 1s for the hollow Pd-CeO₂ NCSs.

Table 1. Compositions of hollow Pd-CeO₂ nanocomposite spheres and supported Pd/CeO₂ catalysts.

Catalyst	Pd(wt%) In solution	XPS		ICP	
		Pd(wt%)	Pd/Ce(atom)	Pd(wt%)	Pd/Ce(atom)
h-Pd-CeO₂-773K	1.5	2.00	0.032	2.15	0.035
h-Pd-CeO₂-873K	1.5	2.76	0.045	1.95	0.032
h-Pd-CeO₂-973K	1.5	4.30	0.065	1.95	0.032
Supported Pd/CeO₂-773K	2.0	6.00	0.097	2.00	0.032

Figure 4b shows Ce 3d XPS spectrum of the hollow Pd-CeO₂ NCSs, in which there are the V (BE

= 882.5 eV), U (901.0 eV) peaks and four (*) satellite peaks (BE = 888.8, 898.4, 907.4, 916.7 eV)

and the V' (885.2 eV), U' (903.5 eV) peaks [44]. These results show that the main valence state of Ce in the hollow Pd-CeO$_2$ NCSs is +4 (V, U and four satellite peaks) with small amount of Ce^{3+} (V' and U' peaks). In the O 1s spectra, the peaks at around 529.2eV and 531.8 eV are ascribed to the lattice oxygen in hollow Pd-CeO$_2$ NCSs and its surface oxygen species, respectively.

The amount of Pd obtained by ICP-AES in hollow Pd-CeO$_2$ NCSs was ~2.15%, and obviously higher than theoretic value of Pd (1.5 wt%) in the synthesis solution (Table 1), indicating that not all Ce^{3+} ions in the solution were converted to CeO$_2$ in the synthesis process. For the sample calcined at 500 °C, the fact that the Pd content obtained by XPS is similar to that by ICP, confirms that Pd evenly distributes in the sample. With an increase in the calcination temperature from 500 to 700 °C, the surface concentration of Pd increases from 2.0 to 4.3 wt.% (by XPS), indicating that high temperature makes Pd enriching on the surface. For the supported Pd/CeO$_2$ catalyst, the surface concentration (6.0 wt%) of Pd is much higher than the Pd loading of 2.0wt.%.

The above-mentioned results show that, using resin polymer spheres as hard template and by the help of the strong interaction between Pd and CeO$_2$, the sandwich-like RF polymer@Pd NPs@CeO$_2$ core-shell structure materials can be efficiently converted to the hollow Pd-CeO$_2$ nanocomposite spheres after simple calcination. CeO$_2$ nanocrystals are closely stacked around the well-dispersed Pd NPs on the shell, thus making that the surface valence state of Pd is highly ionic, rather metallic. In the high-temperature calcination process, no Pd aggregation formed, which demonstrates the efficient shielding effect of shell CeO$_2$ crystals at higher temperatures.

3.2. Catalytic performance of hollow Pd-CeO$_2$ nanocomposite spheres

The catalytic activity of the hollow Pd-CeO$_2$ NCSs were evaluated for the reduction of 4-nitrophenol (4-NP) to 4-aminophenol (4-AP) by excess of NaBH$_4$ under ambient conditions and the oxidation of CO, which have been considered as the typical model reactions to investigate the catalytic activities of the noble metal catalysts in aqueous or gaseous conditions.

It is well known that the 4-NP solution exhibits a strong absorption peak at 317 nm under neutral

or acid environment. However, with the excess of $NaBH_4$ in the solution, the 4-NP ions quickly become the dominant species due to the alkalinity of the solution and relative higher acidity of 4-NP compared with water, thus leading to the H^+ dissociation from 4-NP to react with $NaBH_4$, leaving the 4-NP anions. This is consistent with the peak shifting to 400 nm.

As shown in Figure 6a, when a small amount of catalyst (1.5 mg) was added to the solution, the absorption peak at 400 nm decreased quickly and a new peak at 295 nm appeared simultaneously, which indicates the reduction of 4-NP and formation of the 4-AP product. After ~2 min of the reaction, the absorption intensity at 295 nm reached a maximum and the absorption peak at 400 nm entirely diminished. Meanwhile, the light yellow solution completely faded and became colorless.
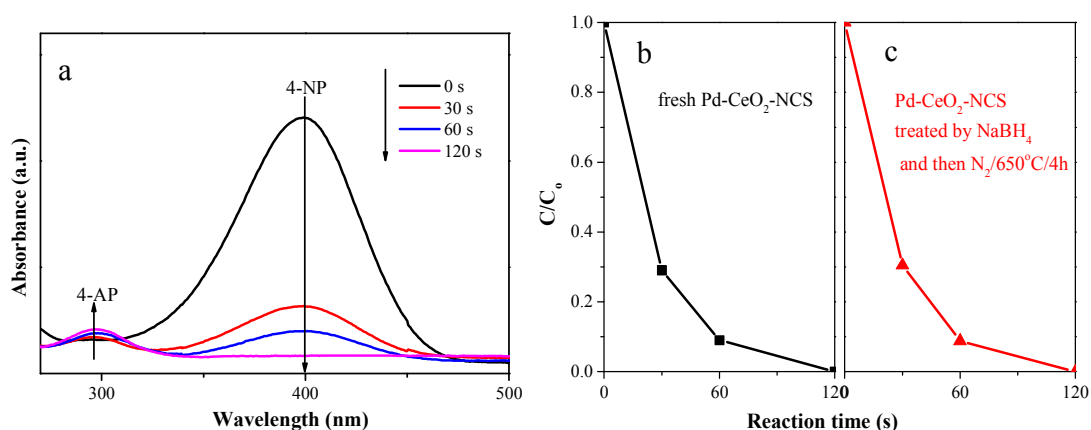

Figure 6. (a) UV-Vis absorption spectra in the reduction of 4-NP to form 4-AP by excess of $NaBH_4$ under ambient condition over the hollow Pd-CeO_2 NCSs, and (b, c) the concentration (C/C_0) of 4-NP as a function of the reaction time over (b) the fresh sample and (c) one treated with $NaBH_4$ and then calcined at 650 °C for 4 h in N_2.

In the selective reduction of 4-NP to 4-AP, Pd acted as the primary active site to catalyze the reduction reaction by facilitating the electron transfer from BH_4^- to the reactant, thus leading to the effective reduction of nitro group[45]. In order to clarify the chemical valence of Pd active sites in the reaction process, we did one experiment without 4-NP reactant, but only the excess $NaBH_4$, in which other experiment conditions were remained. The results show that, when the hollow Pd-CeO_2 NCSs catalyst was added to the solution under stirring for a few seconds, the color of this catalyst changed from brown to grayish, which is caused by the reduction of Pd^{2+} to metallic Pd.
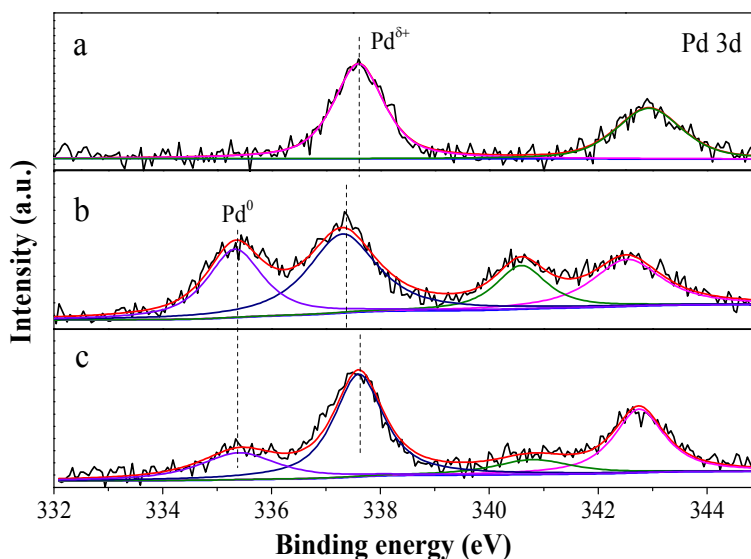
Figure 7. Pd 3d XPS spectra of hollow Pd-CeO$_2$ nanocomposite (a) calcined at 500 °C, (b) after treated by NaBH$_4$, and (c) after CO oxidation.

As shown in Figure 7a, the XPS spectrum of *in situ* reduced sample exhibits only two peaks at about 335.3 eV and 340.2 eV, indicating the formation of metallic Pd species by the reduction of partial Pd^{2+} ions. Therefore, we propose that the highly catalytic activity of the hollow Pd-CeO$_2$ NCSs is attributed to these metallic Pd clusters on the surface of CeO$_2$ crystallites. Besides, the core-shell structural features can enhance the synergistic effect between the Pd NPs and the CeO$_2$ NPs and speed up the charge transfer rate, resulting in an increase in the catalytic activity [46]. To test the thermal-resistant stability of these h-Pd-CeO$_2$ NCSs, we further treated the reduced sample at 650 °C in N$_2$ for 4 h, and then its catalytic activity for the 4-NP reduction was tested under the same condition. Comparing with the catalytic activity of fresh catalyst (Figure 6b), after the sample was treated with NaBH$_4$ then calcined at 650 °C in N$_2$ for 4 h, its catalytic activity remained unchanged (Figure 6b), that is, the conversion of 4-NP to 4-AP could be completed for ~2 min. As shown in the TEM images of this reduced and thermally treated sample, its structure and shape could be well maintained (Figure S6), indicating the good chemical and thermal stability of this Pd-CeO$_2$ NSCs catalyst.
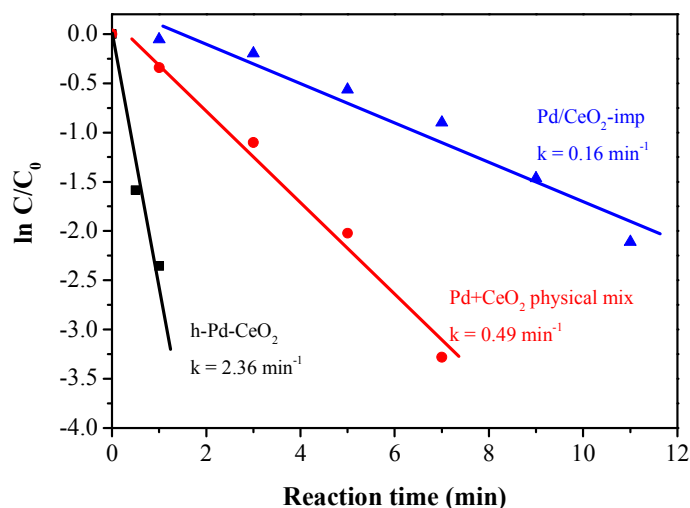
Figure 8. ln(C/C$_0$) as a function of the reaction time (t) over hollow Pd-CeO$_2$ NCSs, Pd/CeO$_2$-imp and Pd + CeO$_2$ physical mixture catalyst for the reduction of 4-NP to 4-AP by excess of NaBH$_4$ under ambient condition.

For a comparison, the catalytic activity of Pd/CeO$_2$-imp catalyst prepared by impregnation method and the physical mixture of Pd + CeO$_2$ catalyst were also tested under the abovementioned experiment conditions. The 4-NP conversion can be directly seen from the ln (C/C$_0$) (C is the concentration of 4-NP at reaction time (t) and C$_0$ is the initial concentration of 4-NP) versus the reaction time (t), which is shown in Figure 8. Evidently, two reference catalysts possess inferior catalytic performance compared with the h-Pd-CeO$_2$ NCSs. For the reduction of 4-NP with excess of NaBH$_4$, CeO$_2$ behaves no catalytic activity. Therefore, the catalytic performances of these samples are strongly affected by the size of Pd nanoparticles and their states in the reaction system. As shown in the TEM image of Figure S7, for the physical mixture of Pd + CeO$_2$ catalyst calcined at 500 °C without the purposeful design of the core-shell hollow structure, agglomeration of Pd nanoparticles occurs, thus, the available surface area of active Pd would decrease obviously, resulting in the reduction of its catalytic activity. As for the Pd/CeO$_2$-imp catalyst, though no bare Pd particles are seen in the TEM images, the Pd species are not evenly distributed on whole CeO$_2$ support (Figure S8). The XPS analysis indeed exhibits a peak at 336.6 eV, which could be attributed to the formation of PdO species (Figure S9). Besides, most of Pd/CeO$_2$-imp particles are severely sintered (Figure S8) and the sample cannot be well dispersed in 4-NP solution. The catalyst powder

15

would quickly deposit at the bottom of the reaction vessel during the catalytic reaction, which limits

the efficient contact between the reactants and Pd sites in solution, resulting a remarkable reduction

of its catalytic activity.

The above results show that, the structures of the catalyst and active Pd states indeed affect their

catalytic performances. Among three catalysts, the Pd NPs in hollow Pd-CeO$_2$ NCSs could be well

protected by CeO$_2$ nanocrystals in the shell, thereby preserving its high catalytic activity. And the

porous CeO$_2$ shell and the hollow structure could favor the diffusion of reactants and products, and

increase the efficient contact between reactants and the Pd active sites, leading to an enhancement

of the catalytic performance. TOF of the h-Pd-CeO$_2$ NCSs was calculated and reached 335 h^{-1},

which shows good catalytic activity compared with the catalysts reported (Table 2).

Table 2. TOF values over the supported Pd catalysts for the reduction of 4-NP.

Catalyst	TOF (h^{-1})[*]	Ref.
Pd/PPy/TiO$_2$	32.3	47
Pd-spherical polyelectrolyte brushes	159	48
@Pd/CeO$_2$	1068	31
Core-shell Pd@hCeO$_2$	300	32
Pd/Polymer/CNT	96	49
h-Pd-CeO$_2$	335	This work

Figure 9a shows the relationship of $\ln(C/C_0)$ versus the reaction time (t) over the h-Pd-CeO$_2$

NSCs catalyst with different amounts. An almost linear evolution between $\ln(C/C_0)$ and time (t)

indicates a first-order reaction for the concentration of 4-NP. When the catalyst amount is 1.5 mg

(0.038 mg$_{Cat.}$/mL), the reduction rate of 4-NP is closed to that over 2.2 mg catalyst (0.055

mg$_{Cat.}$/mL); decreasing the catalyst concentration would dramatically decrease the catalytic reaction

rate, and further increasing the catalyst concentration hardly affects the catalytic reaction rate

obviously, so the appropriate catalyst amount is about 0.038 mg$_{Cat.}$/mL. As shown in Figures 8 and

9, the reduction of 4-NP to 4-AP by excess of NaBH$_4$ under ambient condition is one order reaction

for 4-NP concentration, hence, the rate constant k can be calculated from the rate equation $\ln(C/C_0)$

16

= −kt.

Figure 9b shows the effect of the calcination temperature on the catalytic activity of h-Pd-CeO$_2$ NCSs catalyst. As shown in the plots of ln(C/C$_0$) versus the reaction time, the catalytic activity of this catalyst increases slightly after being calcined at 700 °C, this is because that the surface concentration of Pd species was increased after calcination at higher temperature (Table 1). It is interesting that the Pd nanoparticles in the h-Pd-CeO$_2$ NCSs did not aggregate even after being calcined at 700 °C and its catalytic activity could be well maintained.
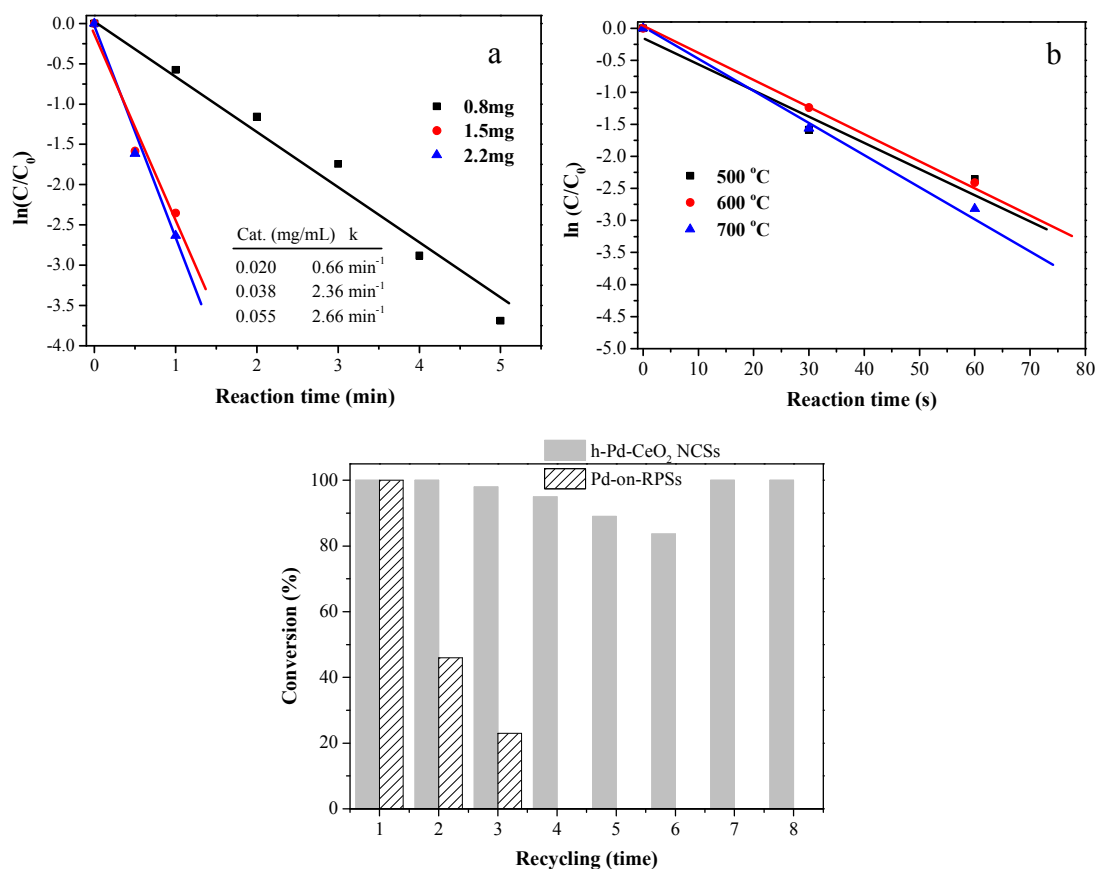

Figure 9. Plots of ln(C/C$_0$) *vs* the reaction time (t) over the hollow Pd-CeO$_2$ NCSs catalyst (a) with 0.8~2.2 mg (calcined at 500 °C), (b) with 1.5 mg (calcined at 500~700 °C), and (c) the conversion of 4-NP (4 min) *vs* recycling times over the h-Pd-CeO$_2$ NCSs calcined at 500 °C and Pd-on-resin polymer spheres (RPSs) catalysts (1.5 mg) for the reduction of 4-NP to 4-AP by excess of NaBH$_4$ under ambient condition.

Figure 9c shows the effect of recycling use on the catalytic activity of h-Pd-CeO$_2$ NCSs. With the increase of the recycling times, the conversion of 4-NP dropped gradually, and the conversion of 4-NP reached 84% after 6 times of recycling use. Notice that the h-Pd-CeO$_2$ NCSs catalyst was

17

reclaimed from solution by centrifugation before reuse, in which some nano-composites cannot be reclaimed due to its excellent dispersing in water, and only about 50% of h-Pd-CeO$_2$ NCSs could be obtained after 6 cycles. When this recovered catalyst was replenished to 1.5 mg by adding fresh catalyst, its catalytic conversion can reach 100% once again in the 7th and 8th run. The TEM image (Figure S10) shows that the morphology of the Pd-CeO$_2$ NCSs after 5 times of recycling use could be well maintained, though some hollow spheres are broken, and the ICP analysis shows that its Pd amount is about 1.9 wt%, that is to say, almost no leaching of Pd species occurs after recycling use 5 times. These phenomena verify that it is the weight loss during the separation process rather than degradation of catalyst, which is the reason for the decrease of the catalytic conversion with the increasing recycling times.

Moreover, we prepared the catalyst of Pd NPs supported on the resin polymer spheres (denoted as Pd-on RPSs), and its catalytic performance for the reduction of 4-NP to 4-AP by excess of NaBH$_4$ under ambient condition was tested. The results (Figure 9c) show that after being repeatedly used 3 times, the catalytic activity of Pd-on RPSs decreases dramatically, probably due to the detachment of Pd NPs from the resin polymer spheres.

The Pd supported on CeO$_2$ is one of the most prevalent catalysts in the exhaust emission control, so the catalytic performance of hollow Pd-CeO$_2$ NCSs catalyst for CO oxidation was also evaluated. Typically, 30 mg of h-Pd-CeO$_2$ NCSs was loaded in a U-type quartz tubular reactor, the gas mixture of 1%CO-20%O$_2$/N$_2$ was used as the feed gas, and the space velocity was 100,000 mL/(g$_{cat}$·h).

As shown in Figure 10a, the h-Pd-CeO$_2$ NCSs possess a good catalytic activity for CO oxidation in high space velocity of 100,000 mL/(g$_{cat}$·h), and the calcination temperature affects its catalytic activity, for instance, the sample calcined at 700 °C exhibits a higher catalytic activity than the sample calcined at 500 or 600 °C. This situation is consistent with the catalytic reduction of 4-NP over this h-Pd-CeO$_2$ NCSs catalyst, which should be attributed to the higher surface concentration of Pd species on the sample calcined at 700 °C (Table 1).

A cycling test was conducted to study the stability of the h-Pd-CeO$_2$ NCSs catalyst at different

temperatures, in which the reaction was tested at 600 °C for 30 min, and then the reaction temperature was cooled to 130 °C to evaluate the CO oxidation for 30 min, and then repeatedly the cycling operation above. As seen in Figure 11, after alternate reaction at 600 °C and 130 °C three times, the h-Pd-CeO$_2$ NCSs still maintain around 80% CO conversion at 130 °C. As shown its TEM image (Figure S11), its original structure can be well kept after being used alternately at 600 °C and 130 °C three times, indicating its high and stable catalytic performance at higher reaction temperature.
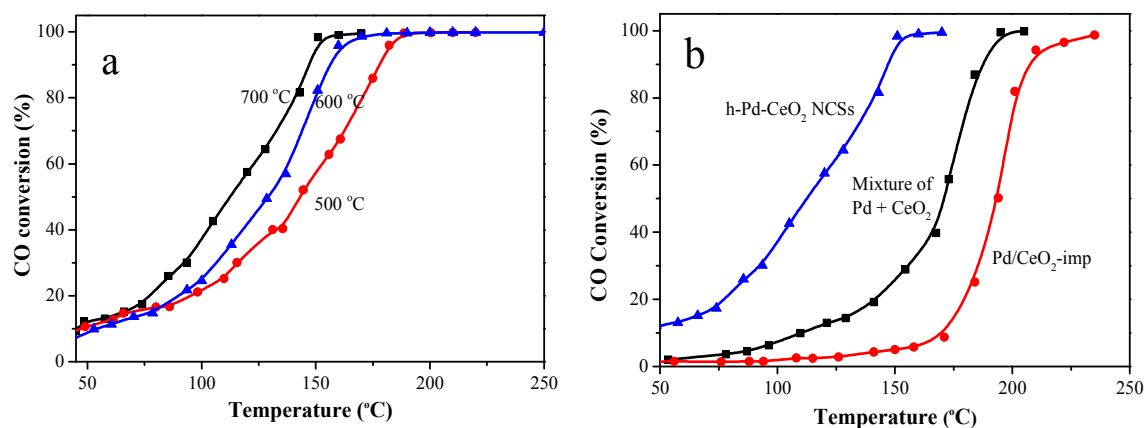

Figure 10. CO oxidation over (a) h-Pd-CeO$_2$ NCSs calcined at 500-700 °C, and (b) h-Pd-CeO$_2$ NCSs, Pd/CeO$_2$-im and physical mixture of Pd + CeO$_2$ (Space velocity of 100,000 mL/(g$_{cat}$·h)).
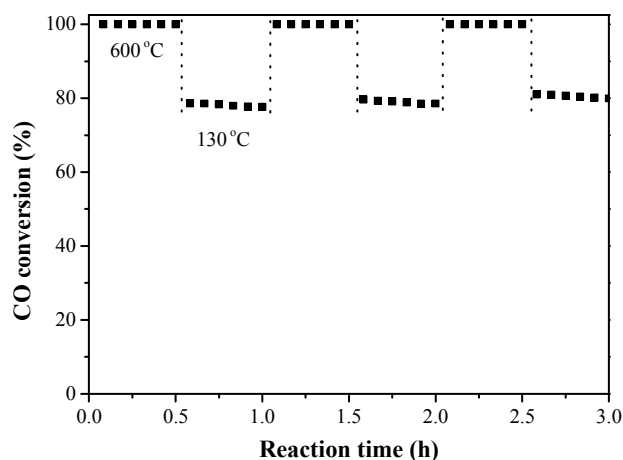

Figure 11. CO oxidation over the h-Pd-CeO$_2$ NCSs catalyst at alternate change of 600 °C and 130 °C (Space velocity of 100,000 mL/(g$_{cat}$·h))

The catalytic activities of three Pd catalysts for CO oxidation are shown in Figure 10b. The activity of h-Pd-CeO$_2$ NCSs catalyst is much higher than these of Pd/CeO$_2$-imp and the physical

mixture of Pd + CeO_2 catalysts. Based on the differences in the textural and physicochemical properties of three catalysts, the higher activity of h-Pd-CeO_2 NCSs catalyst for the CO oxidation might be closely related to the size of Pd NPs, the surface area of catalyst and the interface between Pd and CeO_2[50-52]. In the h-Pd-CeO_2 NCSs, the Pd NPs are uniformly scattered in the ceria shell and no aggregation occurs after calcination at high temperature. Besides, a comparatively higher surface area of h-Pd-CeO_2 NCSs would be beneficial to the improvement of its catalytic activity.

The larger Pd particles detached from the nanosized CeO_2 can be observed in the mixture of Pd + CeO_2 catalyst, due to sintering at high temperature. For the Pd/CeO_2-imp catalyst, the surface area and TEM testing have confirmed a low surface area and unevenly distribution of PdO particles on the sample. These disadvantages result in their poor catalytic activities at low temperature (below 120 °C).

In the h-Pd-CeO_2 NCSs, the electron exchange occurs at the interface between Pd NPs and nanosized CeO_2, and the surface Pd species is ionic, as evidenced in the Pd 3d XPS profile. To maintain the charge neutrality, the oxygen vacancies should be created at the CeO_2 near Pd NPs, leading to the partial reduction of CeO_2 to CeO_{2-x}, because of lower valence state of Pd^{2+} compared with the Ce^{4+}. Therefore, we can conclude that the Pd^{2+} ions at the interface are the active sites for CO adsorption, and the neighboring oxygen vacancies can facilitate the adsorption and activation of gaseous O_2 to form peroxide (O_2^{2-}) species [53], thus the CO oxidation could occur at lower temperature. And the O1s XPS spectra in Figure S12 clearly shows that, the h-Pd-CeO_2 NCSs has a higher ratio of surface chemisorbed oxygen (531.8 eV) to lattice oxygen (529.2 eV) than that of the supported Pd/CeO_2-imp catalyst. More chemisorbed oxygen species would be beneficial to the reaction with the absorbed CO molecules on nearby interfacial Pd^{2+} species, which could well improve the catalytic activity for the CO oxidation. After this catalyst was used in the CO oxidation, the valence state of Pd is mostly still in a form of ionic state (Figure 7c). Two new tiny peaks at EB = 335.3eV and 340.5 eV in its Pd 3d XPS spectrum showed the formation of metallic Pd^0 species, which might be caused by the reduction of CO [39].

20

4. Conclusions

In summary, we have successfully prepared a hollow Pd-CeO$_2$ nanocomposite spheres (NCSs) via a simple polymer-template method. The Pd nanoparticles (NPs) in the feedstock solution have closely stacked in the surrounding CeO$_2$ nanocrystals after eliminating the template core, that is to say, the Pd NPs are highly dispersed inside the CeO$_2$ shell in this prepared hollow Pd-CeO$_2$ NCSs materials, and would not aggregate even after being calcined at 700 °C and its structure and catalytic performance could be well maintained. The confined shield effect of CeO$_2$ shell can efficiently inhibits the aggregation of Pd NPs and prevents the leaching of Pd species in the solution reaction. Besides, the surface Pd species in hollow Pd-CeO$_2$ NCSs is mainly ionic, which is caused by the electron exchange between Pd atoms and their surrounding CeO$_2$ nanocrystals in the calcination process. Therefore, the synergistic catalytic effect between Pd NPs and CeO$_2$ can be enhanced in this core-shell like structure.

For the aqueous-phase selective reduction of 4-nitrophenol to 4-aminophenol and gas phase low temperature oxidation of CO, this hollow Pd-CeO$_2$ NCSs material shows the excellent catalytic activity and reusability, compared with supported Pd/CeO$_2$ catalyst and the physical mixed catalyst of Pd + CeO$_2$. The synthetic strategy herein might provide a novel guidance in desigin and fabricating muti-core@oxide shell core-shell nanocomposite that can act as effective multifunctional nanoreactors in a variety of research fields.

Reference

[1] K. Serp and K. Philippot, *Nanomaterials in Catalysis*, Wiley-VCH, 2012.

[2] D.Astruc, F. Lu and J. R. Aranzaes, *Angew. Chem. Int. Ed.*, 2005, **44**, 7852-7872.

[3] W. Yu, Marc D. Porosoff and J. G. Chen, *Chem. Rev.*, 2012, **112**, 5780-5817.

[4] G. H. Hutchings and C. J. Kiely, *Acc. Chem. Res.*, 2013, **46**, 1759-1772.

[5] S. Linic, P. Christopher, X. Hong and A. Marimuthu, *Acc. Chem. Res.*, **2013**, 46, 1890-1899.

[6] Y. Xia, X. Xia, Y. Wang and S. Xie, *MRS Bull.*, 2013, **38**, 335-344.

[7] Q.L. Zhu, J. Li and Q, Xu, *J. Am. Chem. Soc.*, 2013, **135**, 10210-10213.

[8] T. W. Hansen, A. T. DeLaRiva, S. R. Shalla and A. K. Dayte, *Acc. Chem. Res.*, 2013, **46**, 1720-1730.

[9] R. Ouyang, J. Liu and W. Li, *J. Am. Chem. Soc.*, 2013, **135**, 1760-1771.

[10] M. Pérez-Lorenzo, B. Vaz, V. Salgueiriño and M. A. Correa-Duarte, *Chem.-Eur. J.*, 2013, **19**, 12196-12211.

[11] H. C. Zeng, *Acc. Chem. Res.*, 2013, **46**, 226-235.

[12] Y. Deng, Y. Cai, Z. Sun, J. Liu, C. Liu, J. Wei, W. Li, C. Liu, Y. Wang and D. Zhao, *J. Am. Chem. Soc.*, 2010, **132**, 8466-8473.

[13] J. Ge, Q. Zhang, T. Zhang and Y. Yin, *Angew. Chem. Int. Ed.*, 2008, **47**, 8924-8928.

[14] Y. Dai, B, Lim, Y. Yang, C. M. Cobley, W. Li, E. C. Cho, B. Grayson, P. T. Fanson, C. T. Campbell, Y. Sun and Y. Xia, *Angew. Chem. Int. Ed.*, 2010, **49**, 8165-8168.

[15] P. Lu, C. T. Campbell and Y. Xia, *Nano Lett.*, 2013, **13**, 4957-4962.

[16] Q. Zhang, I, Lee, J. B. Joo, F. Zaera and Y. Yin, *Acc. Chem. Res.*, 2013, **46**, 1816-1824.

[17] G. Li and Z. Tang, *Nanoscale*, 2014, **6**, 3995-4011.

[18] J. Lu, B. Fu, M. C. Kung, G. Xiao, J. W. Elam, H. H. Kung and P. C. Stair, *Science*, 2012, **335**, 1205-1208.

[19] L. Shang, T. Bian, B. Zhang, D. Zhang, L. Wu, C. Tung, Y. Yin and T. Zhang, *Angew. Chem. Int. Ed.*, 2014, **53**, 250-254.

[20] Z. Sun, H. Zhang, Y. Zhao, C. Huang, R. Tao, Z. Liu and Z. Wu, *Langmuir*, 2011, **27**, 6244-6251.

[21] C. T. Campbell, *Nat. Chem.*, 2012, **4**, 597-598.

[22] A. Bruix, J. A. Rodriguez, P. J. Ramírez, S. D. Senanayake, J. Evans, J. B. Park, D. Stacchiola, P. Liu, J. Hrbek and F. Illas, *J. Am. Chem. Soc.*, 2012, **134**, 8968-8974.

[23] P. Hu, Z. Huang, Z. Amghouz, M. Makkee, F. Xu, F. Kapteijn, A. Dikhtiarenko, Y. Chen, X. Gu and X. Tang, *Angew. Chem. Int. Ed.*, 2014, **53**, 3418-3421.

[24] N. Ta, J. Liu, S. Chenna, P. A. Crozier, Y. Li, A. Chen and W. Shen, *J. Am. Chem. Soc.*, 2012, **134**, 20585-20588.

[25] J. Paier, C. Penschke and J. Sauer, *Chem. Rev.*, 2013, **113**, 3949-3985.

[26] N. Acerbi, S. Golunski, S. H. Tsang, H. Daley, C. Hardacre, R. Smith and P. Collier, *J. Phy. Chem. C*, 2012, **116**, 13569-13583.

[27] C. Sun, H. Li and L. Chen, *Energy Environ. Sci.*, 2012, **5**, 8475-8505.

[28] Y. Jiao, F. Wang, X. Ma, Q. Tang, K. Wang, Y. Guo and L. Yang, *Microporous and Mesoporous Mater.*, 2013, **176**, 1-7.

[29] N. C. Strandwitz and G. D. Stucky, *Chem. Mater.*, 2009, **21**, 4577-4582.

[30] C. Y. Cao, Z. M. Cui, C. Q. Chen, W. G. Song, and W. Cai, *J. Phys. Chem. C*, 2010, **114**, 9865-9870.

[31] B. Liu, S. Yu, Q. Wang, W. Hu, P. Jing, Y. Liu, W. Jia, Y. Liu, L. Liu and J. Zhang, *Chem. Commun.*, 2013, **49**, 3757-3759.

[32] N. Zhang and Y. J. Xu, *Chem. Mater.*, 2013, **25**, 1979-1988.

[33] J. Liu, S. Z. Qiao, H. Liu, J. Chen, A. Orpe, D. Zhao and G. Q. Lu, *Angew. Chem. Int. Ed.*, 2011, **50**, 5947-5951.

[34] T. Teranishi and M. Miyake, *Chem. Mater.*, 1998, **10**, 594-600.

[35] S. Guo, S. Dong and E. Wang. *ACS Nano*, 2010, **4**, 547-555.

[36] H. Sun, J. He, J. Wang, S. Y. Zhang, C. Liu, T. Sritharan, S. Mhaisalkar, M. Y. Han, D. Wang and H. Chen, *J. Am. Chem. Soc.*, 2013, **135**, 9099-9110.

[37] K. Noack, H. Zbinden and R. Schlögl, *Catal. Lett.*, 1990, **4**, 145-155.

[38] S. Hinokuma, H. Fujii, M. Okamoto, K. Ikeue and M. Machida, *Chem. Mater.*, 2010, **22**, 6183-6190.

[39] K.R. Priolkar, P. Bera, P. R. Sarode, M.S. Hegde, S. Emura, R. Kumashiro and N.P. Lalla, *Chem. Mater.*, 2002, **14**, 2120-2128.

[40] M.S. Hegde, G. Madras and K. C. Patil, *Acc. Chem. Res.*, 2009, **42**, 704-712.

[41] B. Basu, S. Das, P. Das, B. Mandal, D. Banerjee and F. Almqvist, *Synthesis*, 2009, **7**, 1137-1146.

[42] B. Basu and S. Paul, *Appl. Organometal. Chem.*, 2013, **27**, 588-594.

[43] S. Zhang, C. Chen, M. Cargnello, P. Fornasiero, R. J. Gorte, G. W. Graham and X. Pan, *Nat. Commun.*, 2015, **6**, 7778-7784.

[44] G.J. Wang, Y. Guo and G.Z. Lu, *Fuel Processing Technology*, 2015, **130**, 71-77.

[45] S. Praharaj, S. Nath, S.K. Ghosh, S. Kundu and T. Pal, *Langmuir*, 2004, **20**, 9889-9892.

[46] T. Yu, J, Zeng, B. Lim and Y. Xia, *Adv. Mater.*, 2010, **22**, 5188-5192.

[47] X. Liu, X. Bian, G. Nie, C. Zhang, C. Wang and Y. Wei, *J. Mater. Chem.*, 2012, **22**, 12723-12730.

[48] Y. Mei, Y. Liu, F. Polzer, M. Ballauff and M. Drechsler, *Chem. Mater.*, 2007, **19**, 1062-1069.

[49] H. Li, L. Han, J. Cooper-White and I. Kim, *Green Chem.*, 2012, **14**, 586-591.

[50] A.I. Boronin, E.M. Slavinskaya, I.G. Danilova, R.V. Gulyaev, Yu.I. Amosov, P.A. Kuznetsov, I.A. Polukhina, S.V. Koscheev, V.I. Zaikovskii and A.S. Noskov, *Catal. Today*, 2009, **144**, 201-211.

[51] R.V. Gulyaev, A.I. Stadnichenko, E.M. Slavinskaya, A.S. Ivanova, S.V. Koscheev and A.I. Boronin, *Appl. Catal. A: Gen.*, 2012, **41**, 439-440.

[52] M. Cargnello, V.V.T. Doan-Nguyen, T.R. Gordon, R.E. Diaz, E.A. Starch, R.J. Gorte, P. Fornasiero and C.B. Murray, *Science*, 2013, **341**, 771-773.

[53] H.Y. Li, H.F. Wang, X.Q. Gong, Y.L. Guo, Y. Guo, G.Z. Lu and P. Hu, *Phys. Review B*, 2009, **79**(19), 193401-4